Analysis of Coordinated Steering Performance in Multi-wheel Landing Gears

GUI Xiwen[1], *ZHANG Ming*[1,2*], *SHI Xiazheng*[1], *HU Tianyang*[1], *XU Yuhan*[1]

1. State Key Laboratory of Mechanics and Control for Aerospace Structures, Nanjing University of Aeronautics and Astronautics, Nanjing 210016, P. R. China;

2. Key Laboratory of Fundamental Science for National Defense-Advanced Design Technology of Flight Vehicle, Nanjing University of Aeronautics and Astronautics, Nanjing 210016, P. R. China

(Received 12 June 2025; revised 30 September 2025; accepted 15 October 2025)

Abstract: During aircraft ground steering, the nose landing gear (NLG) tires of large transport aircraft often experience excessive lateral loads, leading to sideslip. This compromises steering safety and accelerates tire wear. To address this issue, the rear landing gear is typically designed to steer in coordination with the nose wheels, reducing sideslip and improving maneuverability. This study examines how structural parameters and weight distribution affect the performance of coordinated steering in landing gear design for large transport aircraft. Using the C-5 transport aircraft as a case study, we develop a multi-wheel ground steering dynamics model, incorporating the main landing gear (MLG) deflection. A ground handling dynamics model is also established to evaluate the benefits of coordinated steering for rear MLG during steering. Additionally, the study analyzes the impact of structural parameters such as stiffness and damping on the steering performance of the C-5. It further investigates the effects of weight distribution, including the center-of-gravity (CG) height, the longitudinal CG position, and the mass asymmetry. Results show that when the C-5 employs coordinated steering for rear MLG, the lateral friction coefficients of the NLG tires decrease by 22%, 24%, 26%, and 27%. The steering radius is reduced by 29.7%, and the NLG steering moment decreases by 19%, significantly enhancing maneuverability. Therefore, in the design of landing gear for large transport aircraft, coordinated MLG steering, along with optimal structural and CG position parameters, should be primary design objectives. These results provide theoretical guidance for the design of multi-wheel landing gear systems in large transport aircraft.

Key words: multi-wheel landing gear; coordinated steering; aircraft ground steering dynamics; influence law analysis

CLC number: V226 **Document code:** A **Article ID:** 1005-1120(2025)05-0659-20

0 Introduction

Modern large transport aircraft have an extremely high takeoff weight. For safe operation through airport runways, the number of landing gear tires must be increased to reduce the radial load on each tire. Currently, heavy-load aircraft typically use either a multi-wheel and multi-strut landing gear layout or a conventional tricycle configuration, where multiple wheels are mounted under a single MLG strut. Replacing a single large wheel with multiple smaller wheels improves the aircraft's ground handling and maneuverability[1]. The multi-wheel and multi-strut landing gear offers several advantages. It effectively reduces the impact on runways during landing and taxiing turns, which is especially important for heavy aircraft. Additionally, the presence of multiple struts distributes axial forces more evenly, reducing the load on each strut. This design also decreases stress on key structural components, such as fuselage frames and wing spars[2]. Transport aircraft, due to their significant weight and the need to operate on various runway conditions, commonly adopt a multi-wheel, multi-axle landing gear layout.

*Corresponding author, E-mail address: zhm6196@nuaa.edu.cn.

How to cite this article: GUI Xiwen, ZHANG Ming, SHI Xiazheng, et al. Analysis of coordinated steering performance in multi-wheel landing gears[J]. Transactions of Nanjing University of Aeronautics and Astronautics, 2025,42(5):659-678.

http://dx.doi.org/10.16356/j.1005-1120.2025.05.009

This design can minimize runway pressure and ensure a more balanced load distribution within the aircraft structure. As a result, it enhances the safety of both takeoff and landing[3]. The C-5A military transport aircraft is equipped with a total of five landing gear struts. The nose landing gear (NLG) features a single row of four wheels arranged side by side. The main landing gear (MLG) consists of four fuselage-mounted struts, each supporting a six-wheel triangular bogie. The main landing gear MLG retracts inward after a 90° hydraulic-actuated rotation[4]. Similarly, Boeing's B747-8 features a four-axle, 16-wheel MLG design, where each axle bears an equal load. This configuration ensures even pressure distribution on the runway during takeoff and landing, improving overall operational safety[5-7].

Steering performance is a key indicator of a transport aircraft's maneuverability. The ground motion characteristics of an aircraft generally refer to its geometric, kinematic, and dynamic behavior during ground operations. With the rapid advancement of modern aircraft design concepts, there is an increasing emphasis on improving both flight performance and quality, namely, the aircraft's airborne motion characteristics. And the requirements for ground motion characteristics have become more stringent. Currently, ground motion characteristics are considered essential evaluation criteria in numerous aircraft design standards and airworthiness regulations. They are now mandatory inspection items in the aircraft certification process[8-12]. The dynamic characteristics of an aircraft during steering are particularly complex. To optimize steering performance and enhance stability, researchers have conducted extensive studies. Barnes et al.[13] developed a six-degree-of-freedom (6-DOF) aircraft taxiing dynamics model and evaluated the aircraft's ground steering and lateral motion performance. Gamez et al.[14] developed an inverted pavement system and a conventional flexible pavement structure, both designed to support a single tire of the A380 landing gear. Their study examined how asymmetric pavement characteristics affect tire stability during steering. Although these studies analyzed the dynamic response of lateral loads during aircraft steering, they did not explore the impact of MLG deflection on steering performance in multi-strut aircraft during maneuvering turns. Although increasing the number of tires significantly enhances an aircraft's shock absorption capability, large transport aircraft typically have a large steering radius. Therefore, MLG participation in steering is necessary to improve maneuverability during ground taxiing[15]. An aircraft's large-angle steering capability reduces runway occupancy time and decreases runway width requirements, significantly enhancing maneuverability and operational efficiency. In general, higher steering speeds and smaller steering radii improve large-angle steering performance. However, these conditions can also increase the risks of sideslip, rollover, and excessive load on the landing gear[16-17]. Hou et al.[18] analyzed the ground motion state of a tricycle landing gear aircraft using a time-domain simulation method. Their study investigated the safe range of steering radii at different speeds. Khapane[19] presented simulations of asymmetric landing cases and typical ground operations for large transport aircraft. The study emphasized that accurately determining static and dynamic loads during ground operations is crucial in the design phase. Compared to real aircraft testing, simulating critical operational scenarios provides a more cost-effective approach for analyzing these loads[19-20]. In recent years, the technology of virtual prototypes (VP) based on multibody system dynamics has gradually matured and been applied to commercial software. By combining vibration theory with multibody system dynamics, this technology effectively studies and analyzes the dynamic behavior of landing gears. The use of such software can significantly shorten analysis time and improve efficiency and accuracy. Additionally, it helps reduce costs and minimizes the risks associated with hazardous operating conditions[21]. By applying VP technology to establish accurate multi-wheel and multi-strut aircraft landing gears, and full aircraft models, ground condition simulations can be conducted to gain in-depth insights into the aircraft's ground loads and landing gear performance. Mosby[7] systematically studied the ground loads of the C-5A aircraft under multi-cycle, multi-strut landing gear con-

ditions using the power spectral density method. The study covered dynamic loads of the aircraft under one-cos single excitation and dual excitation conditions, with a detailed discussion on the selection of one-cos runway wavelength. Additionally, the study examined the impact of aerodynamics on dynamic loads and MLG loads. To meet the requirements of large military/civil aircraft performing multi-wheel and multi-strut steering maneuvers on narrow surfaces, a series of control measures are typically necessary. These measures include increasing the nose wheel steering angle, using asymmetric engine thrust, applying differential braking on the MLG, and selecting appropriate maneuvering speeds to effectively reduce the steering radius. However, if these measures are not applied correctly, they may cause the aircraft to fail to complete the turn successfully, especially a U turn, where performance may be inadequate[22-23]. Yin et al.[24] studied the effects of asymmetric engine thrust on ground steering stability. They employed a numerical continuation method based on bifurcation theory to investigate how structural asymmetry influences aircraft taxiing directional stability. Directional instability during taxiing may be exacerbated by asymmetric fuselage, engine thrust, runway excitations, and various external asymmetric disturbances. Song et al.[25] developed an aircraft ground taxiing model to examine the impact of pitch angle on directional instability during high-speed taxiing. Liang et al.[26] constructed a dynamic model of an aircraft equipped with a taxiing device and analyzed the influence of asymmetric braking moments on taxiing directional stability.

Although extensive studies have been conducted on aircraft ground steering performance, several limitations still exist. Most studies focus on the static and dynamic load analysis of multi-wheel landing gears during ground operations, as well as the improved shock-absorbing capability caused by an increased number of tires. However, there is a lack of in-depth analysis of the dynamic response of multi-wheel and multi-strut landing gear under complex operating conditions and the coordinated steering performance of the main gear and the NLG.

Therefore, this study focuses on the C-5 aircraft and develops a dynamic model that comprehensively considers the coordinated steering of the rear MLG. The analysis evaluates the benefits of this steering approach in terms of key performance indicators, including the steering radius, the nose wheel steering torque, and the friction coefficient. Based on the coordinated steering of the rear MLG, the study further investigates the effects of structural parameters such as stiffness and damping on the steering performance of the C-5. Additionally, it examines the impact of weight distribution parameters, including the center of gravity height, the longitudinal center of gravity position, and the mass asymmetry of the fuselage. The findings provide a theoretical basis for the design of multi-wheel landing gear systems.

1 Establishment of the C-5 Coordinated Steering Dynamics Model

This study establishes a common multi-wheel landing gear layout based on the C-5 aircraft configuration. To facilitate the description of tire load distribution, the numbering of each tire is shown in Fig.1. The C-5 features a dual-wheel NLG located beneath the forward fuselage. The MLG is positioned in the rear half of the fuselage, with two sets on each side. Each set consists of three steerable wheel axles, and each axle holds two parallel-mounted tires. That is, there are a total of 24 tires (12 on each side).

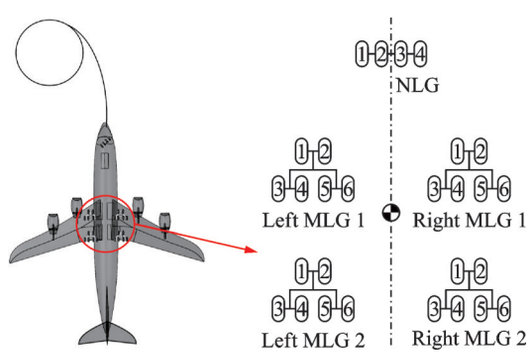

Fig.1 Tire numbering diagram

1.1 Mechanical model of the buffer

During the landing roll, the buffer plays a criti-

cal role in absorbing the impact loads generated upon touchdown. The C-5 uses a conventional oil-gas buffer to dissipate these forces, protecting the aircraft structure and cargo from damage. High-performance buffer enhance landing stability by reducing vibration amplitude, which improves passenger comfort and safety.

The axial force of the buffer Q_V, which is the axial load during its operation, is primarily composed of the following components: The frictional force F_f from the buffer, the damping force F_{oil} generated by oil flow restriction through the orifice, the air spring force F_{air} generated by the compression of the gas chamber, and the structural limit force F_{stp} when the piston rod reaches the limit of its active stroke. The calculation formula is as

$$Q_V=\begin{cases}K_{st}S_M & S_M<0\\ F_{air}+F_{oil}+F_f & \text{Otherwise}\\ K_{sc}(S_M-S_{max}) & S_M>S_{max}\end{cases} \tag{1}$$

where K_{st} and K_{sc} are the tensile stiffness and compressive stiffness of the buffer support, which are related to the structural limit force; S_{max} is the maximum stroke of the buffer and S_M the compression displacement of the buffer.

For a single-chamber oil-gas buffer, the air spring force F_{air} can be calculated as

$$F_{air}=A_a\left[p_0\left(\frac{V_0}{V_0-A_aS}\right)^{\nu}-p_{atm}\right] \tag{2}$$

where p_0 is the initial air pressure in the gas chamber; p_{atm} the local atmospheric pressure at the airport; A_a the piston rod's gas compression area; and ν the gas polytropic index, which is taken as $\nu=1.1$ in this study.

The oil damping force F_{oil} can be calculated as

$$F_{oil}=\begin{cases}\dfrac{\rho A_h^3\dot{S}^2}{2C_d^2A_d^2}+\dfrac{\rho A_{hs}^3\dot{S}^2}{2C_{ds}^2A_n^2} & \dot{S}\geqslant 0\\ -\dfrac{\rho A_h^3\dot{S}^2}{2C_{d1}^2A_{d1}^2}-\dfrac{\rho A_{hs}^3\dot{S}^2}{2C_{ds}^2A_{n1}^2} & \dot{S}<0\end{cases} \tag{3}$$

where A_d and A_{d1} are the cross-sectional areas of the main oil holes during the forward and reverse strokes, respectively; C_d and C_{d1} the flow restriction coefficients of the main oil holes during the forward and reverse strokes, respectively; A_{hs} and C_{ds} the effective oil pressure areas and the flow restriction coefficients of the return oil chamber, respectively; and A_n and A_{n1} the total area of the oil holes in the return oil chamber during the forward and reverse strokes, respectively.

The structural limiting force F_{stp} is calculated as

$$F_{stp}=\begin{cases}K_sS & S<S_0\\ 0 & S_0\leqslant S<S_{max}\\ K_s(S-S_{max}) & S\geqslant S_{max}\end{cases} \tag{4}$$

where K_s is the structural limiting stiffness of the damper in tension and compression; S_{max} the maximum compression stroke of the damper; and S_0 the stroke when the damper is fully extended.

1.2 Tire mechanical model

1.2.1 Tire lateral force modeling

The calculation of the lateral force is based on the normal force and the slip angle. The lateral force is approximated by a cubic function, which is determined by the boundary conditions

$$\alpha=0,\ F_{lat}=0$$
$$\alpha=0,\ \frac{\partial F_{lat}}{\partial\alpha}=C_\alpha$$
$$\alpha=\alpha_n,\ F_{lat}=(F_{lat})_{max}$$
$$\alpha=\alpha_n,\ \frac{\partial F_{lat}}{\partial\alpha}=0$$

where α is the slip angle; α_n the saturation slip angle; F_{lat} the lateral force; $dF_{lat}/d\alpha$ the slope of the lateral force curve with respect to the slip angle; $(F_{lat})_{max}$ the maximum lateral force; and C_α the cornering stiffness.

The saturation slip angle is approximated as

$$\alpha_n=2.5\cdot\frac{F_{norm}}{C_\alpha} \tag{5}$$

The maximum lateral force is the product of the nominal coefficient of friction and the normal force, expressed as

$$F_{lat}=\max(F_{lat})=\mu\cdot F_{norm} \tag{6}$$

where μ is the nominal friction coefficient.

The relationship between the lateral force and the slip angle is shown in Fig.2.

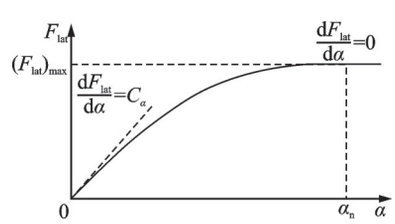

Fig.2 α-F_{lat} relationship diagram

The slip angle is defined as the angle between the tire center heading vector and the tire velocity vector projection in the terrain tangent plane. Since the slip angle is always acute, the sign of the slip angle is dependent on the sign of the lateral velocity component of the tire center. This definition alleviates the need for logic to account for a change in direction of the tire.

Therefore, the slip angle is expressed as

$$\alpha = \arctan\left(\left|\frac{V_{\text{lat}}}{\max(V, V_{\text{eps}})}\right|\right) \cdot \text{scale} \tag{7}$$

The proportionality factor is expressed as

$$\text{scale} = \frac{V_{\text{lat}}}{V_{\text{eps}} + |V_{\text{lat}}|} \tag{8}$$

where V is the forward velocity of vehicle; V_{eps}= gravity/400, a small number to prevent division by zero when vehicle comes to rest; and V_{lat} the lateral velocity. The scale factor helps prevent stiffness of the equations at small lateral velocity.

1.2.2 Tire normal force modeling

The tire normal force is calculated in one of the following two ways.

(1) Point contact

The normal deflection and velocity are computed using a point contact, wheel-ground interaction model that assumes a ground profile that has the shape of a locus of points traced by the wheel center of a rigid wheel rolling over the actual terrain profile. This is the wheel center locus terrain profile. The normal force is then applied in a direction normal to this terrain profile.

(2) Distributed contact

The normal deflection and velocity are computed based upon the intersection of the undeformed tire circle and the terrain profile, but also include the effects of any sharp points in the profile. The tire circle is divided into a user-defined number of vertical "slice" (Note: The number of slices should be sufficiently large to accurately account for the smallest feature of interest in the road profile). For each slice, the vertical positions of the two points at the corners of the slice are compared with the terrain height at the same horizontal positions. If the points on the tire circle lie below the terrain, the area of intersection A_i is found using a simple trapezoidal rule. Once the total intersected area is found, an equivalent normal deflection δ is found by first finding θ, and the half-angle of the chord satisfies

$$\sum A_i = r^2\theta - r^2\cos\theta\sin\theta \tag{9}$$

$$\delta = r - r\cos\theta \tag{10}$$

The point of application of the tire force C_p is found through a weighted average of the centroids of the partial intersected areas

$$C = \frac{\sum A_i C_{pi}}{\sum A_i} \tag{11}$$

Likewise, the direction of the force is found through a weighted average of the terrain gradient vectors associated with the partial intersected areas

$$g = \frac{\sum A_i g_i}{\left|\sum A_i g_i\right|} \tag{12}$$

The intersected area is then checked for any local features (sharp points). If these features rise sufficiently above the nominal surface, their effect is added to the equivalent deflection and gradient using a separate weighting scheme. The schematic diagram of the normal force on the tire is shown in Fig.3.

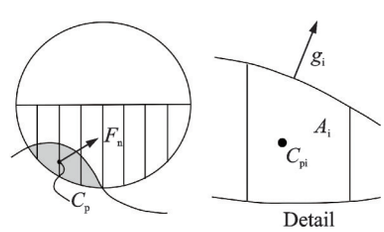

Fig.3 Tire normal force diagram

Roads can use existing road elements. If no terrain profile enters, either in the road or tire element, the road is assumed flat in the global X-Y plane and located at zero in Z. The terrain tangent plane is defined to be the plane tangent to the terrain profile at the point-of-contact between tire and terrain. The longitudinal and lateral forces are computed in this plane, and are assumed to act in this plane.

The terrain tangent plane coordinate system is defined by these rules: Z''' axis of the terrain tangent plane coordinate system is normal to the tangent plane, directed upwards; X''' axis is the intersection of the terrain tangent plane and the plane of the tire

disk.; Y''' axis is in the terrain tangent plane, perpendicular to X''' axis, directed so that a right-handed coordinate system results.

1.2.3 Modeling of tire hitch trail

The front turn moment is calculated by multiplying the sum of the front lift stability distance and the front lift rear drag distance with the front lift lateral force. This method provides a more accurate estimation of the front turn moment, closely reflecting the real value. The relevant calculation formula follows the NASA-TR-64 semi-empirical model. To calculate the rear drag distance, it is necessary to know the tire compression, the half-length of the tire contact patch, the tire slip angle, and the vertical load on the tire. As shown in Fig.4, the schematic diagram of the tire contact patch semi-major axis is presented.

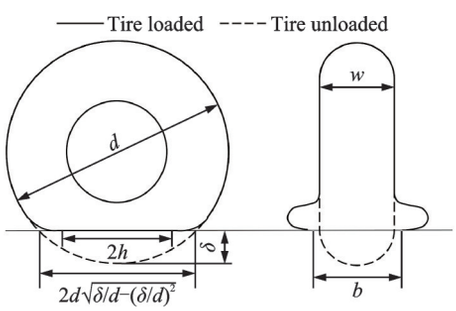

Fig.4 Tire contact patch semi-major axis diagram

The semi-major axis h of the tire footprint is calculated as

$$h/d = 0.85\sqrt{\delta/d + (\delta/d)^2} \tag{13}$$

where d is the tire diameter and δ the vertical compression of the tire.

Fig.5 shows the schematic diagram of the tire slip angle.

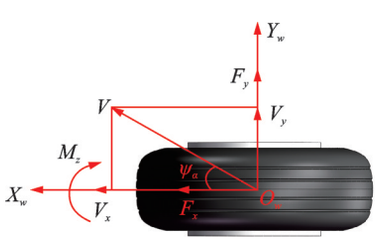

Fig.5 Tire slip angle diagram

The tire slip angle ψ is calculated as

$$\psi = \arctan\frac{V_y}{V_x} \tag{14}$$

The trail distance q is calculated as

$$q = M/F \tag{15}$$

$$\begin{cases} q = h\times 0.8\Big/\left(1-\dfrac{4}{27}\varphi^2\right) & \varphi\leqslant 0.1 \\ q = h\times(\varphi-\varphi^2-0.01)\Big/\left(\varphi-\dfrac{4}{27}\varphi^3\right) & 0.1<\varphi\leqslant 0.55 \\ q = h\times(0.292\,5-0.1\varphi)\Big/\left(\varphi-\dfrac{4}{27}\varphi^3\right) & 0.55<\varphi\leqslant 1.5 \\ q = h\times 0.292\,5-0.1\varphi & \varphi>1.5 \end{cases} \tag{16}$$

where φ is the trail distance coefficient, and it is calculated as

$$\varphi = \frac{N_m\times\psi}{\mu_g\times F_z} \tag{17}$$

where ψ is the tire slip angle; μ_g the ground friction coefficient; F_z the tire vertical load; N_m the tire slip stiffness, and its calculation is as

$$\begin{cases} \dfrac{N_m}{57(p+0.44p_r)w^2} = 1.2(\delta/d)-8.8(\delta/d)^2 \\ \qquad \delta/d\leqslant 0.087\,5 \\ \dfrac{N_m}{57(p+0.44p_r)w^2} = 0.067\,4-0.34(\delta/d) \\ \qquad \delta/d>0.087\,5 \end{cases} \tag{18}$$

where w is the tire width; p the tire nominal inflation pressure; and p_r the tire actual inflation pressure.

1.3 Ground maneuvering dynamics model

1.3.1 Establishment of the mathematical model

The aircraft's ground maneuvering during steering is primarily executed by the NLG control system, which performs the steering operation. During the steering process, the nose wheels must be precisely rotated to the specified angle and then locked in position. Afterward, the aircraft undergoes fixed-axis rotation around its instantaneous center of rotation.

As shown in Fig.6, the force distribution acting on the aircraft during a left-turn maneuver is illustrated. In this study, the resultant force of the dual wheels under each landing gear strut is concentrated at the wheel axle center due to the relatively small wheel track.

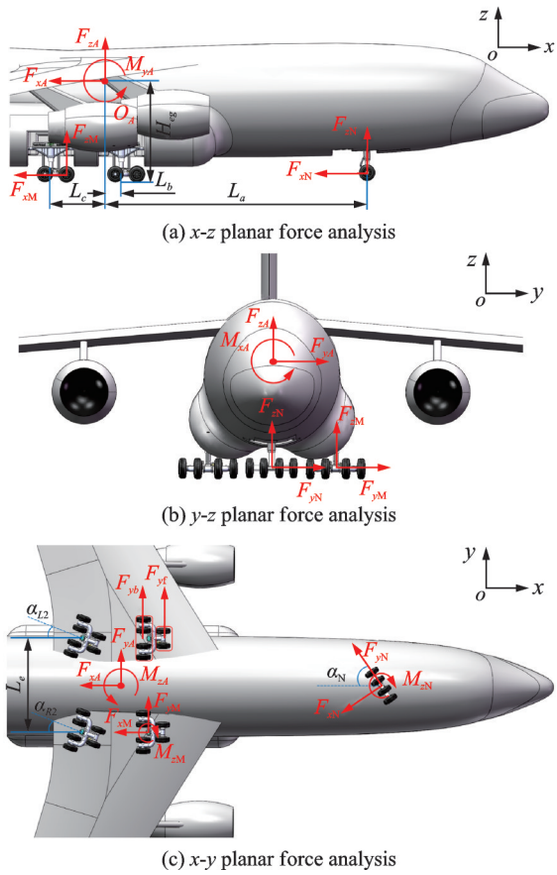

Fig.6 Analysis of forces during aircraft steering process

As shown in Fig.6, A—N are the connection points between each landing gear strut and the aircraft fuselage. O_A is the origin of the aircraft body coordinate system. L_a is the longitudinal distance between the NLG and the aircraft's center of gravity. L_b is the longitudinal distance from the first row of MLG to the aircraft's center of gravity. L_c is the longitudinal distance between two adjacent rows of MLG. L_e indicates the lateral distance between the two MLG struts in the same row.

According to D'Alembert's principle, the equations of motion for the landing gear rotation in the aircraft body coordinate system and the yaw motion of the aircraft are given as

$$I_{zN}\ddot{\alpha}_N = M_{zN} + F_{yN}L_{sN} \tag{19}$$

$$F_{yM} = F_{yf} + F_{yb} \tag{20}$$

$$I_{zL1}\ddot{\alpha}_{L1} = M_{zL1} + F_{yfL1}L_{sfL1} + F_{ybL1}L_{sbL1} \tag{21}$$

$$I_{zR1}\ddot{\alpha}_{R1} = M_{zR1} + F_{yfR1}L_{sfR1} + F_{ybR1}L_{sbR1} \tag{22}$$

$$I_{zL2}\ddot{\alpha}_{L2} = M_{zL2} + F_{yfL2}L_{sfL2} + F_{ybL2}L_{sbL2} \tag{23}$$

$$I_{zR2}\ddot{\alpha}_{R2} = M_{zR2} + F_{yfR2}L_{sfR2} + F_{ybR2}L_{sbR2} \tag{24}$$

$$I_{zz}\ddot{\omega}_z = M_{zM} + M_{zN} \tag{25}$$

$$M_{zN} = F_{yN}L_a \tag{26}$$

$$M_{zM} = \sum_{i=1}^{2}(F_{xLi} + F_{xRi})L_e/2 + (F_{yL1} + F_{yR1})L_b + (F_{yL2} + F_{yR2})L_c \tag{27}$$

where I_{zN} is the moment of inertia of the nose landing gear about its support axis; I_{zL1}, I_{zR1}, I_{zL2}, I_{zR2} are the moments of inertia of the four steerable MLG about their respective support axes; I_{zz} is the moment of inertia of the aircraft fuselage about the z-axis; L_{sN} is the stabilizing torque of the steerable NLG; L_{sfL1}, L_{sfR1}, L_{sfL2}, L_{sfR2} are the stabilizing distances of the front two tires for the four steerable MLG; L_{sbL1}, L_{sbR1}, L_{sbL2}, L_{sbR2} are the stabilizing distances of the rear four tires for the four steerable MLG; M_{zM} is the total moment exerted by the MLG at the aircraft's center of gravity; M_{zN} the total moment exerted by the NLG at the aircraft's center of gravity.

1.3.2 Establishment of the simulation model

Through the dynamic simulation platform, the landing gear components are connected using appropriate kinematic pairs based on the actual motion of the aircraft. The primary types of kinematic pairs used include cylindrical pairs, prismatic pairs, revolute pairs, fixed pairs, and spherical pairs.

Since this study focuses on aircraft taxiing turns, during which the landing gear remains deployed and locked and is connected to the fuselage by fixed pairs. The outer cylinder and piston rod of the MLG strut buffer move along the central axis of the strut, so they are connected by cylindrical pairs. Similarly, the outer cylinder and piston rod of the stabilizing damper are also connected by cylindrical pairs. As the C-5 bottom frame, along with the piston rod, can rotate around the top steering platform, a revolute pair is used between the MLG outer cylinder and the steering platform. The upper and the lower torque arms of the NLG are connected to the landing gear strut by revolute pairs. However, since all three components lie in the same plane, one of the revolute pairs is replaced with a spherical pair to avoid over-constraining the system. The final motion relationships between the landing gear components are illustrated in Fig.7.

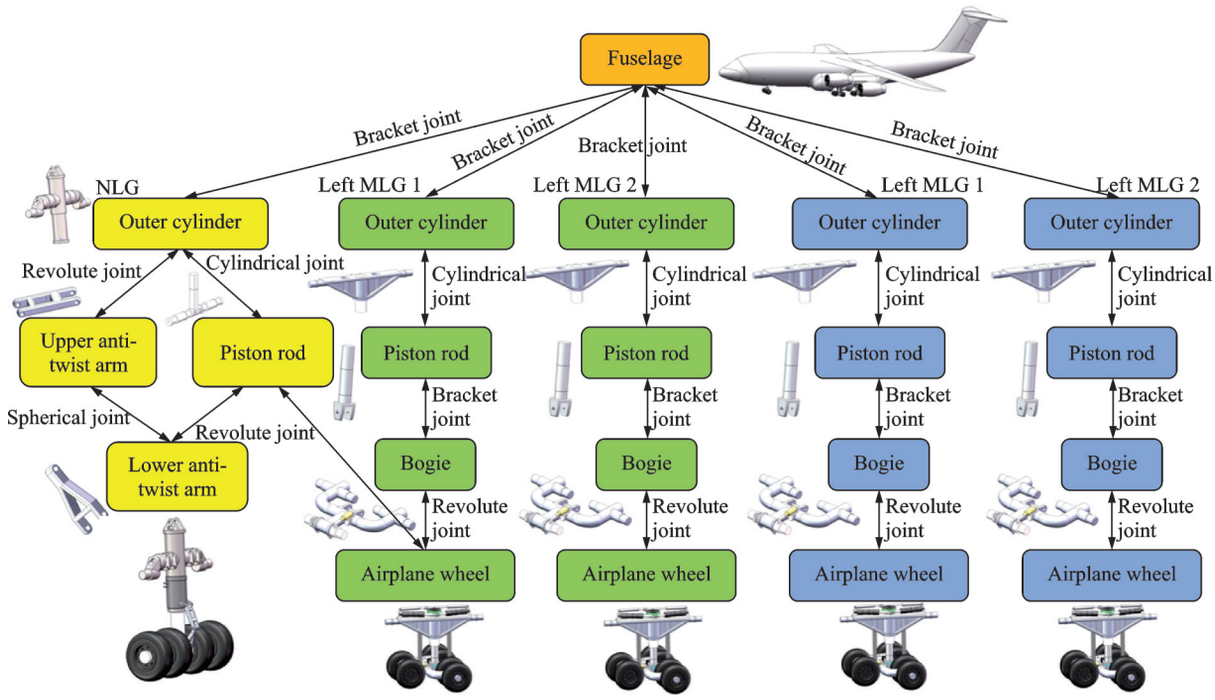

Fig.7 Schematic diagram of the motion relationship between components

Since the structure of the aircraft fuselage is complex and the moment of inertia is difficult to calculate directly, the method of empirical formula estimation is adopted. Considering that the subject of this study is a transport aircraft with a high aspect ratio, the estimation is defined as

$$\begin{cases} I_{xp} = M(b^2/78 + H_F^2/33) \\ I_{yp} = M(L_F^2/29 + H_F^2/33) \\ I_{zp} = M(L_F^2/29 + b^2/78) \end{cases} \tag{28}$$

where I_{xp}, I_{yp}, I_{zp} are the moments of inertia of the aircraft about the x, y, and z axes in the aircraft body coordinate system; b is the wingspan, H_F the fuselage height, and L_F the fuselage length.

The final C-5 full-aircraft dynamic ground steering model is constructed as shown in Fig.8.

Fig.8 Schematic diagram of the C-5 steering kinematic model

The key overall aircraft parameters used in this study are shown in Table 1.

Table 1 Aircraft primary parameters

Parameter	Value
Maximum takeoff mass/kg	418 000
Distance from the center of gravity to the nose gear/mm	21 339
Distance from the center of gravity to the first main gear/mm	1 904
Distance between the front and rear main gears/mm	5 588
Vertical height from the center of gravity to the ground/mm	3 641
Distance between left and right main gears/mm	7 886
Aircraft roll moment of inertia/(kg•m^{-2})	2.97×10^7
Aircraft pitch moment of inertia/(kg•m^{-2})	8.67×10^7
Aircraft yaw moment of inertia/(kg•m^{-2})	1.06×10^8

2 Analysis of Multi-wheel Aircraft Coordinated Steering Performance

2.1 Criteria for successful aircraft steering

The general requirements for an aircraft's ground taxiing turn are as follows. Under normal conditions, neither the nose wheels nor the main wheels should experience slip. In some cases, a small amount of slip in the nose wheels may be allowed. To ensure the aircraft can turn smoothly, it

is necessary to assess the balance between the nose wheel driving torque and the main wheel yawing lateral torque. Specifically, when the nose wheel steering angle is zero, the corresponding torque is also zero. As the nose wheel steering angle increases, the nose wheel driving torque becomes relatively large. Since the slip angle is small, the main wheel yawing torque is also small, allowing the nose wheel driving torque to be greater than the main wheel lateral yawing torque, which enables the aircraft to turn smoothly. As the nose wheel steering angle continues to increase, the nose wheel driving torque starts to decrease, while the main wheel yawing torque increases. Once the nose wheel steering angle exceeds a certain value, the nose wheel driving torque becomes smaller than the main wheel lateral yawing torque, at which point the aircraft will no longer be able to complete the turn.

During the aircraft's ground steering process, the nose wheel steering torque primarily functions to overcome the lateral force experienced by the NLG. As the steering conditions become more demanding, such as when the steering radius decreases or the steering speed increases, the lateral force on the nose wheels gradually increases. To simplify the comparison, this process can be reflected by changes in the tire's lateral friction coefficient.

In this study, we set the maximum lateral friction coefficient to 0.8, which is a theoretical limit, indicating that the friction between the tire and the ground has reached its maximum possible value. When the tire's lateral force increases to its peak value, the lateral friction coefficient also reaches its maximum. At this point, the nose wheel's steering torque can no longer provide enough centripetal force to maintain the turn, meaning that the NLG is at the critical steering state. If the steering conditions continue to worsen, or the nose wheels continue to execute the steering command, the lateral friction coefficient of the tire will start to decrease. This is because the tire can no longer maintain stable contact with the ground under the current lateral force, and the friction force begins to weaken. As the friction coefficient continues to decrease and enters a steady state, the relative motion between the tire and the ground intensifies, eventually leading to the occurrence of slip. Slip indicates that the tire has lost its ability to control the turn and can no longer follow the intended steering trajectory. This phenomenon not only affects the aircraft's steering performance but also leads to increased tire wear and even pose a safety risk to the aircraft's taxiing.

2.2 Analysis of coordinated steering performance

To ensure that the analysis conditions align with actual operational standards, we define the taxi speed limit as the maximum ground speed permitted and required by aircraft operations on taxiways and aprons. According to national military standards, large and heavy aircraft may have two types of taxi speed limits: One for the apron and another for the taxiway. These two should be distinguishable and recognizable by the pilot. The taxi speed limits should be compatible with the aircraft's intended use, as well as the operators' ability to recognize and maintain the aircraft's speed below this limit while on the apron and taxiway. Taking national military standards into account, the aircraft's steering taxi speed is set to 5 m/s (approximately 9.7 knots), which falls into the safe steering speed range of 2.572—5.144 m/s (5—10 knots) and remains constant. During the aircraft's ground steering process, both the steering angle and steering speed are key factors influencing the steering performance. Larger steering angles and higher steering speeds significantly increase the lateral load on the NLG, which brings the tire's lateral force closer to the friction limit and increases the likelihood of slip or even loss of control. Therefore, combinations of large steering angles and high steering speeds are considered extreme conditions, placing high demands on the aircraft's steering performance. Consequently, the aircraft is required to turn left, with the maximum nose wheel steering angle fixed at 35°. This setting aims to simulate typical extreme steering conditions and allow a systematic analysis of how the aircraft's steering performance changes under these conditions, while ensuring that the research results lead to practical engineering applications.

In the study of the improvement in steering performance of the C-5 transport aircraft using a rear main wheel steering mechanism, the tire lateral fric-

tion coefficient is a key indicator. By analyzing the time-dependent changes in the lateral friction coefficient of each tire on the NLG, the effectiveness of the rear wheel steering in mitigating tire slip tendencies can be intuitively reflected. Therefore, Fig.9 displays the dynamic changes in the lateral friction coefficient of each nose tire under different operating conditions.

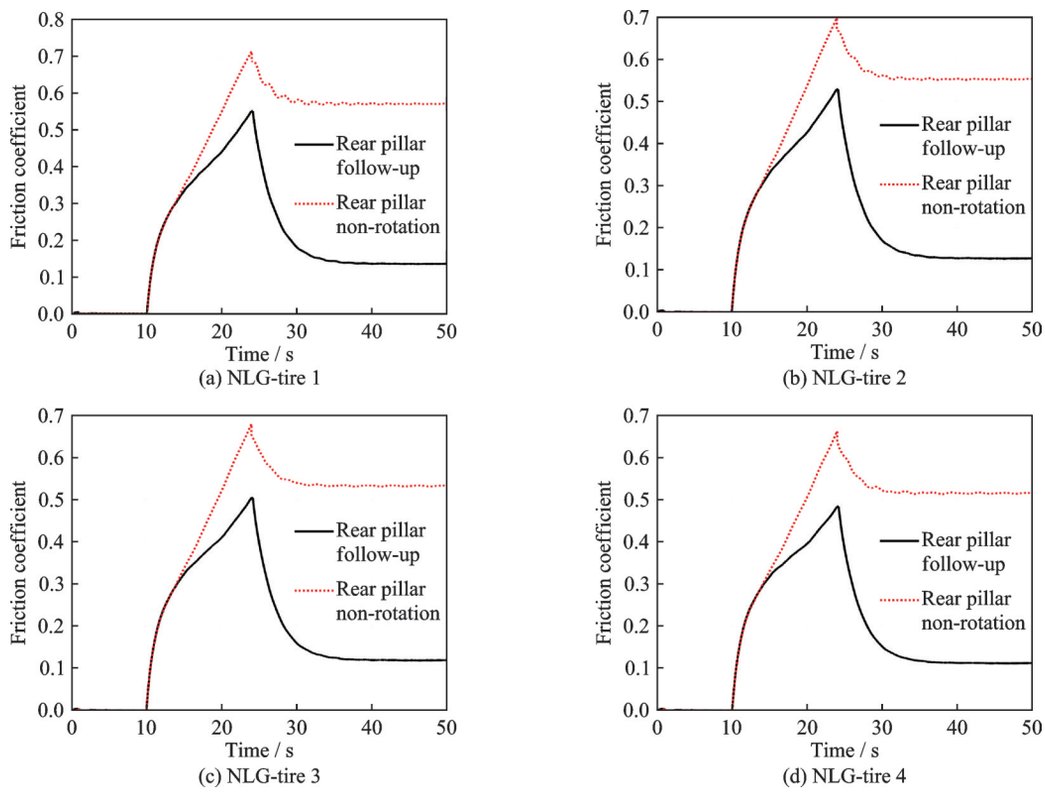

Fig.9 Changes of NLG tire lateral friction coefficients

The results indicate that when the main wheels do not steer, the friction coefficients of the NLG-tire 1—NLG-tire 4 are 0.71, 0.70, 0.68, and 0.66, respectively. After implementing rear main wheel steering, the friction coefficients are reduced to 0.55, 0.53, 0.50, and 0.48, respectively. This demonstrates that the rear main wheel steering significantly reduces the lateral friction coefficient of the NLG tires, which makes it easier for the aircraft to complete the turn command. From the simulation results, it is clear that tire 1 experiences the most severe conditions, so it will be used as the primary subject of study in subsequent analyses.

By analyzing the variation of the nose wheel steering torque with time, we can intuitively understand the dynamic response characteristics of the aircraft during the steering process, as well as the changes in the magnitude of the steering torque. This, in turn, allows for an assessment of the stability and maneuvering efficiency during the turn. Fig.10 shows the variation of the C-5 nose wheel steering torque with time.

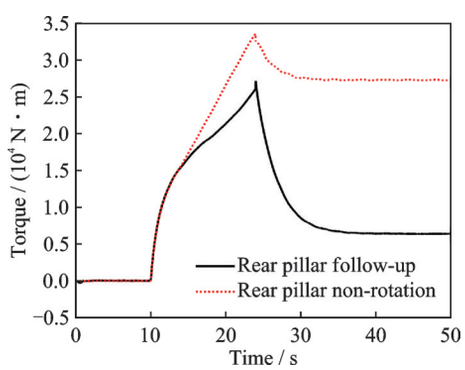

Fig.10 Nose wheel steering torque under the influence of main wheel steering

It can be observed that, when the main wheels do not steer, the aircraft's nose wheel steering torque is 33 545 N·m. After implementing rear main wheel steering, the nose wheel steering torque decreases to 27 160 N·m, indicating that the rear main wheel steering significantly reduces the aircraft's nose wheel steering torque.

By analyzing the variation of the aircraft steer-

ing radius with time, we can clearly observe the dynamic characteristics of the aircraft at different steering stages, as well as the benefits of the rear wheel steering design on the steering radius. This provides important insights for evaluating the aircraft's ground maneuvering performance. Fig.11 shows the variation of the C-5 aircraft steering radius with time.

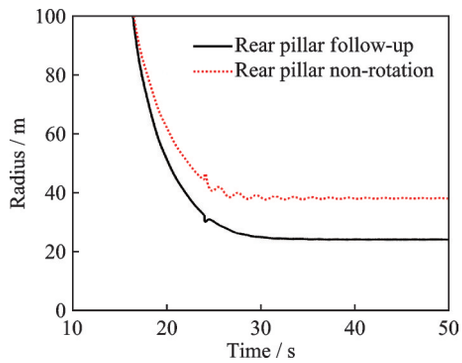

Fig.11 Aircraft steering radius under the influence of main wheel steering

The steering radius extracted in this study refers to the minimum steering radius that the aircraft reaches in a stable steering state. It can be observed that, when the main wheels do not steer, the aircraft's stable steering radius is 38.11 m. After implementing rear main wheel steering, the stable steering radius of the aircraft reduces to 26.76 m. This demonstrates that rear main wheel steering significantly reduces the aircraft's steering radius.

Based on the simulation results, it can be analyzed that the steering performance of the C-5 has been significantly improved after implementing rear main wheel steering. The main benefits are as follows: Under the harsh steering conditions of a 35° maximum nose wheel steering angle and a 5 m/s steering speed, rear main wheel steering effectively addresses the issue of the nose landing gear failing to turn smoothly. The lateral friction coefficients of the nose landing gear tires are reduced by 22%, 24%, 26%, and 27%, making the NLG easier to steer. The aircraft's steering radius is reduced by 29.7%, enhancing its steering maneuverability. The nose wheel steering torque decreases by 19%, which effectively aids in the nose landing gear's steering. These results demonstrate a significant improvement in the aircraft's overall steering capability and ground maneuvering performance.

3 Performance Analysis of Multi-wheel Aircraft Steering Without Main Landing Gear Steering

3.1 Investigation of the influence of aircraft steering speed

This section investigates the influence of the NLG steering speed on the steering performance of the aircraft when the MLG remains non-steerable. The simulation conditions are defined as shown in Table 2, where parameter α_N represents the maximum steering angle of the NLG and parameter v denotes the aircraft steering speed. In Cases 1 to 3, the maximum steering angle of the NLG is fixed at 35°, allowing for an analysis of how variations in steering speed affect the ground maneuvering performance of the C-5 aircraft.

Table 2 Working conditions and results of NLG steering speed

Test condition	Case 1	Case 2	Case 3
α_N/(°)	35	35	35
v/(m•s^{-1})	1	3	5

During the steering process, since the aircraft performs a left turn, the outer NLG tire experiences greater lateral slip compared to the inner tire. As indicated by the analysis in the previous section, the NLG-tire 1 shows the most critical slip condition. Therefore, NLG-tire 1 is selected as the focus for analyzing NLG lateral slip behavior. The variation in the friction coefficient of NLG-tire 1 under Cases 1 to 3 is shown in Fig.12.

Based on the results, the peak friction coefficients of the NLG tire under Conditions 1 to 3 are

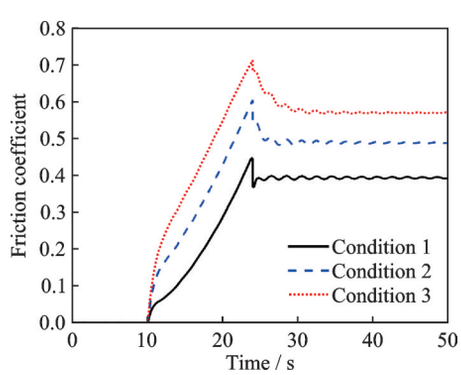

Fig.12 NLG tire lateral friction coefficient under the influence of Conditions 1 to 3

0.44, 0.60, and 0.71, respectively, increasing with the steering speed.

The variation of the nosewheel steering moment under different steering speeds is analyzed. The time histories of the steering moment for NLG-tire 1 under Conditions 1—3 are shown in Fig.13.

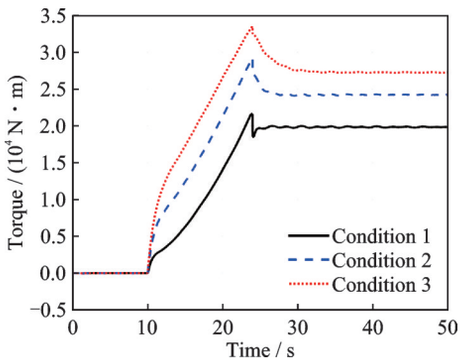

Fig.13 Nose wheel steering torque under the influence of Conditions 1 to 3

Based on the results, the peak steering moments of the NLG under Conditions 1 to 3 are 21 632, 29 285, and 33 469 N·m, respectively, increasing with the steering speed. Among them, Condition 3 yields the highest steering moment.

The variation of the aircraft steering radius under different steering speeds is analyzed. The time histories of the C-5 aircraft steering radius are shown in Fig.14.

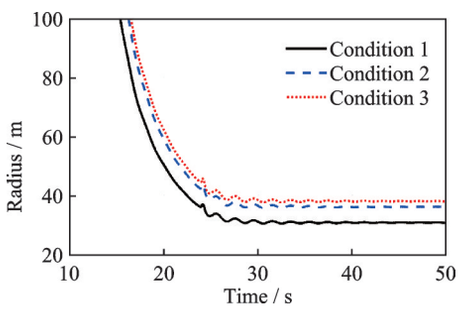

Fig.14 Aircraft steering radius under the influence of Conditions 1 to 3

Based on the results, the steering radii of the aircraft under Conditions 1 to 3 are 30.2, 36.25, and 38.2 m, respectively, increasing with the steering speed.

3.2 Investigation of the influence of aircraft steering angle

This study investigates the effect of nosewheel steering angle on aircraft turning performance when the main landing gear is non-steerable. The simulation conditions are defined in Table 3. The aircraft turning speed is fixed at 5 m/s, and the analysis focuses on how the maximum steering angle of the NLG influences the ground maneuvering performance of the C-5 aircraft.

Table 3 Working conditions and results of the maximum steering angle of the NLG

Test condition	Case 4	Case 5	Case 6
α_N/(°)	25	30	35
v/(m·s^{-1})	5	5	5

The variation in the friction coefficient of NLG-tire 1 under Conditions 4—6 is shown in Fig.15.

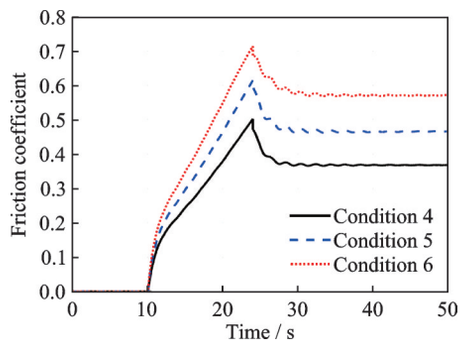

Fig.15 NLG tire lateral friction coefficient under the influence of Conditions 4 to 6

Based on the results, the peak friction coefficients of the nose landing gear tire under Conditions 4 to 6 are 0.50, 0.61, and 0.71, respectively, increasing with the steering angle.

The variation of the nosewheel steering moment under different steering angles is analyzed. The time histories of the steering moment for NLG-tire 1 under Conditions 4—6 are shown in Fig.16.

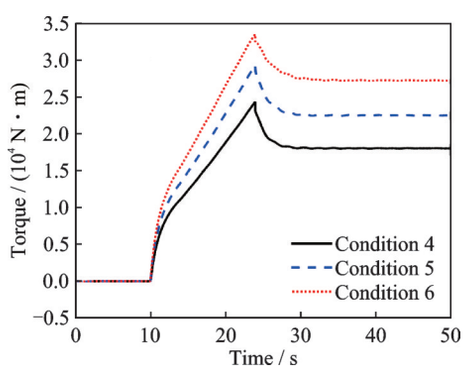

Fig.16 Nose wheel steering torque under the influence of Conditions 4 to 6

Based on the results, the peak steering moments of the nose landing gear under Conditions 4—6 are 24 403, 29 346, and 33 540 N·m, respective-

ly, increasing with the steering angle. Condition 6 exhibits the highest steering moment.

The variation of the aircraft turning radius under different steering angles is analyzed. The time histories of the C-5 aircraft turning radius are shown in Fig.17.

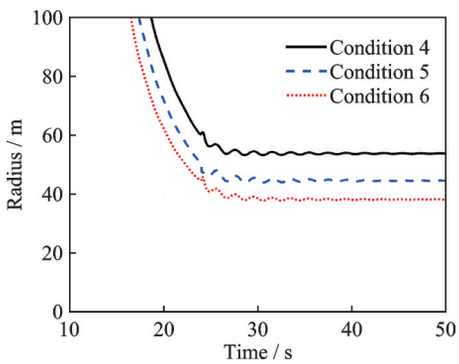

Fig.17 Aircraft steering radius under the influence of Conditions 4 to 6

Based on the results, the steering radii of the aircraft under Conditions 4 to 6 are 53.9, 44.8, and 38.4 m, respectively, decreasing with the increase of the steering angle.

The results show that, regardless of whether the maximum nosewheel steering angle or the steering speed increases, the friction coefficient of the NLG tire exhibits an upward trend. For example, under Conditions 3 and 6, the friction coefficient of the nose tire approaches 0.8, indicating a risk of tire slip. This phenomenon suggests that when steering relies solely on independent control of the nose landing gear, increasing either the steering angle or the steering speed may cause tire slip. Tire slip not only degrades steering performance but may also hinder the aircraft's ability to complete ground turns in a stable and safe manner, thus affecting operational reliability.

4 C-5 Ground Maneuver Steering Performance Influence Analysis

To further analyze the factors influencing the C-5 transport aircraft's ground steering performance, this study systematically investigates the effects of structural parameters and weight distribution parameters on the steering performance. By varying the relevant parameters, the impact on key performance indicators during the steering process is analyzed, including the peak tire lateral friction coefficient, peak lateral force on the NLG, and taxi steering radius. This analysis provides a theoretical basis for optimizing the aircraft's ground maneuvering performance.

In the subsequent analysis, all friction coefficients are referenced to the lateral friction coefficient of the NLG-tire 1 under the most severe left-steering conditions for the NLG. This selection is based on the fact that NLG-tire 1 experiences the maximum lateral force during the turn, and its friction coefficient variation provides the most direct reflection of the aircraft's ground maneuvering performance under extreme conditions. Additionally, the lateral load mentioned in the text specifically refers to the lateral load borne by the NLG strut, which is one of the key factors influencing the aircraft's steering performance.

4.1 Influence of structural parameters

The principle of the rotational spring-damper-actuator (RSDA) is to define the RSDA torque through a combination of stiffness and damping values. The stiffness torque and damping torque can be calculated using constant coefficients. The RSDA can be made to generate torque either bi-directionally, only while in tension, or only when in compression.

When the angle of the kinematic pair exceeds the neutral angle of 0, both the spring and the damper are activated. Once activated, the spring and damper deform from their initial "zero torque" state, thereby providing a reaction torque. The neutral angle is referred to as the threshold angle, which activates the stretching or compression of the spring damper. Fig.18 illustrates a schematic of the RSDA.

One of three modes may be chosen for the RSDA, bi-directional, tension-only, or compression-

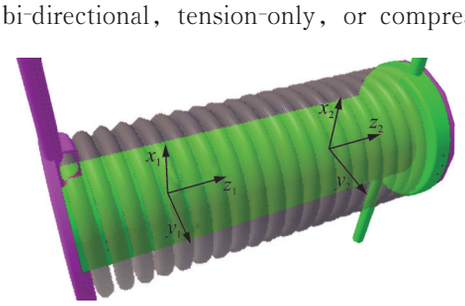

Fig.18 Schematic diagram of rotary spring damper

only. Each mode affects the interpretation of other input variables. The formulation for torque in a bi-directional RSDA is described as

$$\theta = \theta_j - \theta_u \tag{29}$$

$$T_1 = k\theta + c\omega + T_A + T_k(\theta) + T_c(\omega) + T_A(t) \tag{30}$$

$$T_2 = -T_1 \tag{31}$$

where θ is the current angular displacement; θ_j the current angular displacement of the connecting joint; θ_u the undeformed angular displacement of the RSDA defined by the orientation angle variable; k the rotational stiffness constant coefficient; c the rotational damping constant coefficient; ω the relative rotational velocity of Attachment 2 measured in Body 1's reference frame; T_1 the moment applied to Body 1 about the rotational axis of the attachment joint; T_2 the moment applied to Body 2 about the rotational axis of the attachment joint; T_A the constant torque; $T_k(\theta)$ the torque as a function of relative rotation (variable rotational stiffness); $T_c(\omega)$ the torque as a function of relative velocity (variable rotational viscous damping); and $T_A(t)$ the torque as a function of simulation time (variable moment).

In the dynamics model constructed for this study, RSDA are introduced for both rear MLG assemblies to more accurately simulate the C-5 transport aircraft's ground turning characteristics. The specific installation positions and layout are shown in Fig.19. This design aims to optimize the aircraft's dynamic response during ground turning by adjusting the stiffness and damping characteristics of the torsional spring. In the simulation analysis, to ensure accuracy, a constant torque value is set to zero to eliminate any direct interference with the turning performance. Through multiple simulation experiments and data feedback from various operating conditions, an appropriate range for the torsional spring stiffness and damping values is gradually selected, enabling a systematic analysis of the quantifiable impact of these parameters on the aircraft's turning performance.

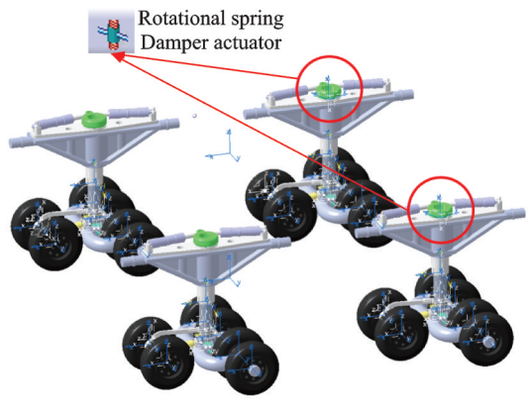

Fig.19 Adding rotary spring dampers to the rear MLG

4.1.1 Stiffness influence analysis

In the design of multi-wheel landing gear, the selection of torsion spring stiffness and damping parameters is crucial. A reasonable torsion spring stiffness improves the aircraft's maneuverability during ground steering, and effectively controls the aircraft's stability and responsiveness under different steering conditions. Through a series of simulation experiments, various stiffness and damping settings are validated, ultimately identifying the key parameters that influence the aircraft's steering performance. After multiple iterative simulation experiments and considering the stability and convergence of the model, the reasonable range for the torsion spring stiffness is determined to be between 1.6×10^5 and 2.16×10^6 N·m/rad. Within this range, the model can effectively reflect the impact of torsion spring stiffness variations on the aircraft's steering performance.

As shown in Table 4, the peak values of the friction coefficient, the NLG lateral force, and the taxiing turning radius under different torsion spring stiffness conditions are presented. The torsion spring stiffness is abbreviated as "Rigidity" in Table 4.

Table 4 Working conditions and results of torsion spring stiffness

Test condition	Case 1	Case 2	Case 3	Case 4	Case 5	Case 6	Case 7	Case 8	Case 9	Case 10	Case 11
Rigidity/ (10^6 N·m·rad^{-1})	0.16	0.36	0.56	0.76	0.96	1.16	1.36	1.56	1.76	1.96	2.16
μ_{max}	0.520	0.630	0.660	0.670	0.680	0.690	0.695	0.697	0.699	0.700	0.710
$F_{y\,max}$/N	103 249	125 850	133 200	136 953	139 021	140 304	141 204	141 910	142 383	142 785	143 200
Radius/m	24.15	31.16	33.63	34.79	35.48	35.93	36.26	36.49	36.68	36.82	36.94

To ensure that the damping parameters minimize the impact of stiffness variations while maintaining the clarity and accuracy of the simulation results, a damping value of 100 N·m·s/rad is selected after multiple verification experiments. This damping value is chosen to ensure that, during the stiffness variation process, the damping's impact on the steering characteristics remains at a low level, thereby highlighting the dominant role of stiffness variations in the steering performance. In the simulation, the aircraft's steering angle is set to 35°, and the steering speed is set to 2.5 (°)/s to simulate typical steering conditions. Additionally, a stepwise approach was used for parameter adjustments during the simulation, ensuring the stability of each indicator. By comparing parameters such as steering radius, lateral force, and friction coefficient at different stiffness values, the optimal range for stiffness and damping settings is ultimately determined.

According to the simulation results shown in Fig.20, as the torsion spring stiffness gradually increases, the peak lateral friction coefficient of the NLG tires shows a significant upward trend, rising from 0.52 to 0.71. At the same time, the peak lateral force on the NLG increases significantly from 1.03×10^5 N to 1.43×10^5 N. Additionally, the aircraft's taxiing steering radius gradually increases as stiffness increases, from 24.1 m to 36.9 m. The simulation results indicate that the torsion spring stiffness has a significant impact on the aircraft's steering performance. As the torsion spring stiffness increases, the peak lateral friction coefficient of the NLG tires rises, while the steering radius also increases. This suggests that while the stiffness improvement increases the nose wheel friction coefficient, it also leads to a decrease in steering agility.

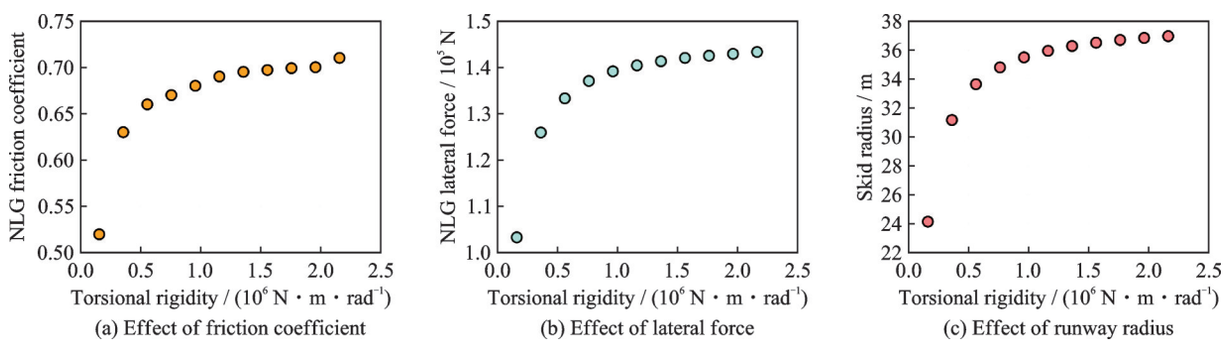

Fig.20 Analysis of the effect of torsion spring stiffness

4.1.2 Damping influence analysis

After multiple iterations of simulation experiments, given the stability and convergence of the model, the reasonable range for the torsional spring damping value is determined to be from 0 N·m·s/rad to 8×10^6 N·m·s/rad. Within this range, the model effectively reflects the impact of changes in torsional spring damping on the aircraft's steering performance.

To minimize the impact of stiffness parameters on the effects of damping variations and to ensure the clarity and accuracy of the simulation results, multiple validation experiments are conducted. As a result, a stiffness value of 1.6×10^5 N·m/rad is selected. This value is chosen to ensure that the influence of stiffness on the steering characteristics remains low during damping variations, thereby highlighting the dominant role of damping in affecting the steering performance.

Table 5 presents the results of peak friction coefficient, peak lateral force at the NLG, and runway steering radius under different RSDA conditions. In the table, rotary spring damping is abbreviated as "Dam".

The simulation results shown in Fig.21 indicate that as the RSDA increases, the peak lateral friction coefficient of the NLG tires exhibits a clear upward trend, increasing from 0.53 to 0.7. Simultaneously, the peak lateral force on the NLG increases significantly from 1.06×10^5 N to 1.42×10^5 N. Additionally, the aircraft's runway steering radius gradually increases with higher damping, from 24.1 m to 31.08 m. These simulation results highlight the significant impact of rotary spring damping on the aircraft's steering performance. Specifically, increasing the damping improves the tire friction coefficient

Table 5 Working conditions and results of RSDA

Test condition	Case 1	Case 2	Case 3	Case 4	Case 5	Case 6	Case 7	Case 8	Case 9
Dam/ (10^6 m^2•kg•s•rad^{-1})	0	1	2	3	4	5	6	7	8
μ_{max}	0.53	0.62	0.66	0.67	0.68	0.69	0.69	0.69	0.70
$F_{y\,max}$/N	106 091	125 065	132 930	136 495	138 693	140 012	140 954	141 697	142 233
Radius/m	24.15	25.43	26.88	26.94	28.00	28.96	29.78	30.49	31.08

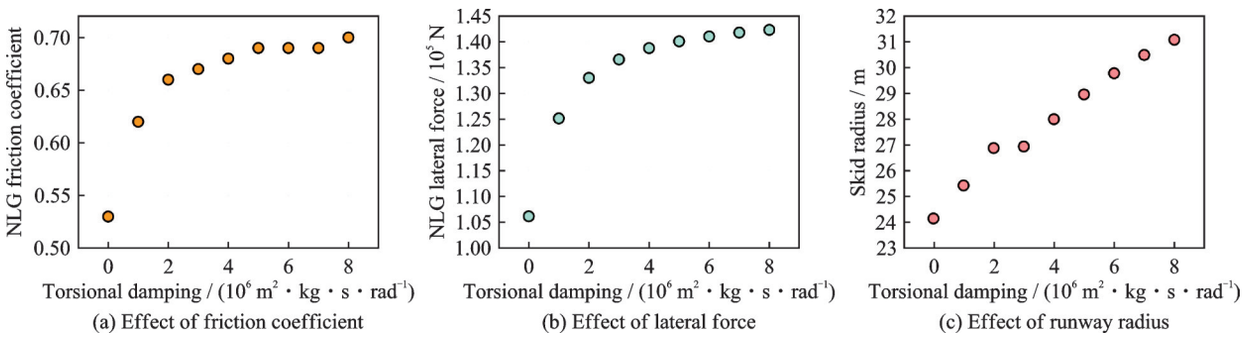

Fig.21 Analysis of the effect of eorsion spring damping

to some extent, while also leading to an increase in the steering radius.

4.2 Influence of weight distribution parameters

Since this section focuses on the impact of the center of gravity distribution parameters on the ground steering performance of the C-5 aircraft, it is essential to eliminate the interference of structural parameters on the simulation results to ensure the accuracy of the research. The variations in the center of gravity distribution parameters should be sufficiently reflected in the steering performance simulation results. Therefore, after multiple simulation tests, the torsion spring stiffness is selected as 200 000 N·m/rad, and the torsion spring damping as 2×10^6 N·m·s/rad as fixed parameters. This ensures that the impact of structural parameters on the steering performance remains at a low level, thus highlighting the effect of the center of gravity distribution parameters.

The center of gravity's forward and aft position in the model is calculated based on the 6∶94 front MLG weight distribution ratio. This ratio reflects the distribution relationship between the NLG and the MLG in the total weight of the aircraft.

4.2.1 Influence of the CG's vertical position

The initial position of the center-of-gravity (CG) in the vertical direction is selected based on engineering experience, with upward being considered as the positive direction and downward as the negative direction. To comprehensively analyze the impact of changes in CG height on steering performance, the range of vertical CG position variation is set from −2 000 mm to 3 000 mm.

As shown in Table 6, the results of the peak friction coefficient, the NLG lateral force peak, and the taxiing turn radius under different CG vertical position conditions are provided. The vertical center of gravity position is abbreviated as CG position in Table 6.

As shown in the simulation results in Fig.22, as the CG height gradually increases, the peak lateral friction coefficient of the aircraft's NLG tires shows a significant upward trend, increasing from 0.64 to 0.70. At the same time, the lateral force

Table 6 Working conditions and results of CG vertical position

Test condition	Case 1	Case 2	Case 3	Case 4	Case 5	Case 6	Case 7	Case 8	Case 9	Case 10	Case 11
CG position/mm	−2 000	−1 500	−1 000	−500	0	500	1 000	1 500	2 000	2 500	3 000
μ_{max}	0.640	0.652	0.655	0.659	0.663	0.667	0.671	0.676	0.680	0.684	0.689
$F_{y\,max}$/N	133 223	133 310	133 377	133 474	133 491	133 579	133 664	133 773	133 780	133 800	133 740
Radius/m	27.145	27.148	27.154	27.159	27.162	27.170	27.175	27.183	27.192	27.202	27.211

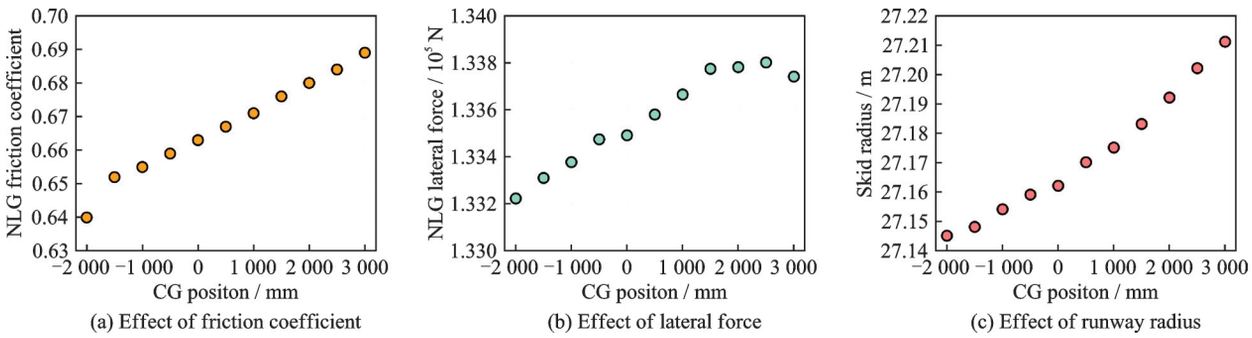

(a) Effect of friction coefficient (b) Effect of lateral force (c) Effect of runway radius

Fig.22 Analysis of the effect of CG vertical position

peak borne by the NLG struts initially increases from 1.332×10^5 N to 1.338×10^5 N as the CG moves upward, and then slightly decreases to $1.336\ 7\times10^5$ N, with a relatively small variation. Additionally, the taxiing turn radius of the aircraft gradually increases from 27.145 m to 27.235 m as the CG height rises. Overall, while the vertical variation of the CG position affects certain performance indicators of the aircraft's steering behavior (such as the lateral friction coefficient and turn radius), the overall impact is relatively small.

4.2.2 Influence of the CG's forward and aft position

The initial position of the model's CG in the fore-aft direction is calculated based on the 6∶94 front-to-MLG weight distribution ratio, which reflects the distribution relationship between the NLG and the MLG in the total aircraft weight. The CG position is calculated relative to the aircraft's longitudinal axis, where the forward direction is positive and the rearward direction is negative. To comprehensively analyze the effect of fore-aft CG variation on steering performance, the variation range for the CG position is set from −600 mm to 600 mm. This range is determined by considering both the actual CG distribution in typical aircraft operations and the extreme conditions during steering maneuvers.

As shown in Table 7, the results of peak friction coefficients, peak lateral forces on the NLG, and steering radii for different CG fore-aft positions are presented. The fore-aft CG positions are abbreviated as "CG position" in Table 7.

According to the simulation results shown in Fig.23, as the CG gradually moves forward, the peak lateral friction coefficient of the NLG tires decreases from 0.79 to 0.61. At the same time, the peak lateral force on the NLG strut increases from 1.07×10^5 N to 1.45×10^5 N as the center of gravity moves forward. Additionally, the aircraft's taxiing steering radius increases from 26.6 m to 27.8 m as the CG shifts forward.

Table 7 Working conditions and results of CG fore-aft position

Test condition	Case 1	Case 2	Case 3	Case 4	Case 5	Case 6	Case 7	Case 8	Case 9	Case 10	Case 11
CG position/mm	−600	−480	−360	−240	−120	0	120	240	360	480	600
μ_{max}	0.79	0.76	0.74	0.70	0.67	0.66	0.65	0.64	0.63	0.62	0.61
$F_{y\,max}$/N	107 266	116 520	121 053	125 939	130 754	133 491	135 920	138 263	140 652	143 174	145 857
Radius/m	26.67	26.75	26.84	26.94	27.04	27.16	27.28	27.41	27.53	27.66	27.79

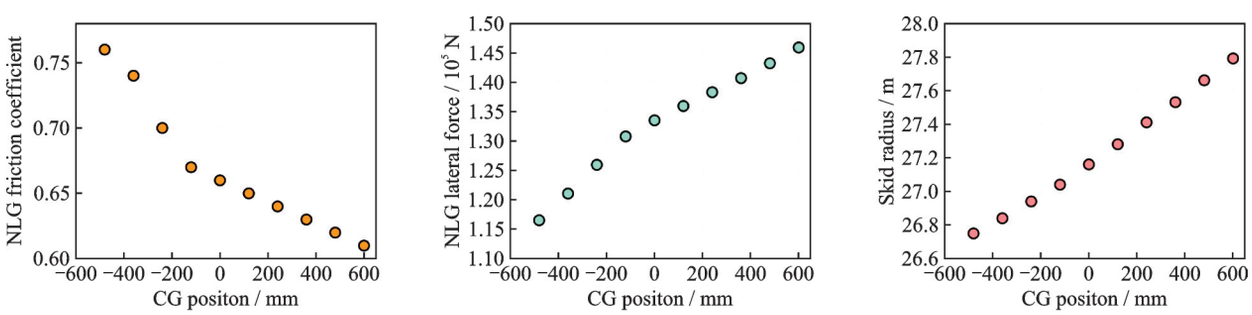

(a) Effect of friction coefficient (b) Effect of lateral force (c) Effect of runway radius

Fig.23 Influence of the CG's forward and aft position

4.2.3 Influence of aircraft's lateral mass asymmetry

Based on the maximum design mass of the latest aircraft model, which is 130 t, it is assumed that the total mass of the mass blocks on both sides of the fuselage is 130 t. However, in actual operations, due to uneven cargo loading, significant asymmetry in the mass distribution between the left and the right sides of the fuselage may occur. This asymmetry mainly results from the non-symmetrical placement of cargo inside the fuselage, leading to an imbalance in the mass distribution between the left and right sides. By setting the left-to-right mass ratio from 1∶0 (all mass concentrated on the left side) to 0∶1 (all mass concentrated on the right side), with incremental adjustments of 0.1 in the right-side mass percentage, a series of simulation scenarios with varying mass distribution ratios were constructed.

As shown in Table 8, the results of peak friction coefficients, peak lateral forces on the nose landing gear, and steering radii during taxiing under different left-to-right mass ratio conditions are provided. The left-to-right mass ratio is abbreviated as "Mass ratio" in Table 8.

As shown in the simulation results in Fig.24, as the mass ratio of the aircraft's outer side during the turn increases, the peak lateral friction coefficient of the NLG tires gradually increases from 0.57 to 0.76. Meanwhile, the peak lateral force on the nose landing gear struts increases from 1.31×10^5 N to 1.34×10^5 N as the center of gravity moves forward. Additionally, the aircraft's steering radius during taxiing increases from 27.07 m to 27.34 m as the outer side mass ratio increases, with a relatively small effect.

Table 8 Working conditions and results of left-to-right mass ratio

Test condition	Case 1	Case 2	Case 3	Case 4	Case 5	Case 6	Case 7	Case 8	Case 9	Case 10	Case 11
Mass ration	1∶0	0.9∶0.1	0.8∶0.2	0.7∶0.3	0.6∶0.4	0.5∶0.5	0.4∶0.6	0.3∶0.7	0.2∶0.8	0.1∶0.9	0∶1
μ_{max}	0.57	0.59	0.60	0.62	0.64	0.66	0.68	0.70	0.72	0.74	0.76
$F_{y\,max}$/N	131 880	132 417	132 735	133 105	133 479	133 770	134 144	134 349	134 451	134 545	134 425
Radius/m	27.074	27.086	27.103	27.122	27.141	27.164	27.191	27.221	27.254	27.294	27.343

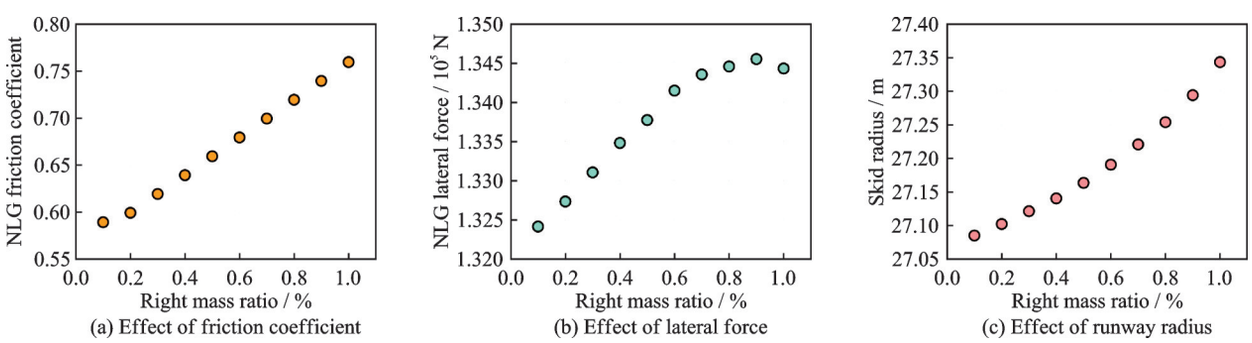

Fig.24 Analysis of the effect of left-right mass distribution ratio

5 Conclusions

(1) This paper focuses on the C-5 aircraft and develops a dynamic model that integrates the coordinated steering of the rear MLG. The steering performance of the aircraft, including key indicators such as steering radius, nose wheel steering torque, and friction coefficient, is analyzed after adopting the coordinated steering method for the MLG. The results show that when the C-5 adopts coordinated steering with the rear main wheels, the aircraft's steering radius, nose gear steering torque, and friction coefficient of the front wheels significantly decrease, leading to a notable improvement in steering performance.

(2) Through a systematic analysis of structural parameters such as stiffness and damping, this study reveals their significant impact on the steering performance of the C-5 transport aircraft. The results show that, when damping remains constant, a smaller torsion spring stiffness can significantly improve steering performance, manifested as a smaller steering radius and lower peak lateral forces. Simi-

larly, when stiffness is fixed, reducing damping also optimizes the steering performance, further validating the critical role of structural parameters in the aircraft's ground maneuvering characteristics.

(3) Through a comparative analysis of simulation results under various conditions, this study examines the impact of weight distribution parameters, such as center of gravity height, forward and aft center of gravity position, and lateral mass asymmetry, on the steering performance. The results show that the variation in the vertical position of the center of gravity has a relatively small overall effect on the aircraft's steering performance; when the center of gravity is positioned more forward, the friction coefficient decreases; when the center of gravity is positioned more aft, the lateral force on the nose gear and the steering radius decrease; and when there is lateral mass asymmetry, better steering performance is observed when the inner steering side has a higher proportion of mass.

References

[1] ZHENG Lan. Design of landing gear scheme for heavy load aircraft[D]. Nanjing: Nanjing University of Aeronautics and Astronautics, 2009. (in Chinese)

[2] YOU Ying. Research on load analysis of multi-wheel multi-strut landing gear[D]. Nanjing: Nanjing University of Aeronautics and Astronautics, 2019. (in Chinese)

[3] FAN Hailong. Research on ground loads of aircraft with multi-wheels and multi-landing gear[D]. Nanjing: Nanjing University of Aeronautics and Astronautics, 2006. (in Chinese)

[4] YANG H. C-5A main landing gear bogie pitching control[J]. Journal of Aircraft, 2017, 8: 912-917.

[5] ZHANG Xianmin, LIU Xiaolan, DONG Qian. Take-off and landing adaptability of A380-800 large aircraft on existing pavement[J]. Journal of Beijing University of Aeronautics and Astronautics, 2016, 42(9): 1812-1818. (in Chinese)

[6] SHI X Z, YU A Y, NIE H, et al. Effects of pitch stabilization buffer on the dynamic performance of frame-type landing gear[J]. Aerospace, 2024, 11(4): 288.

[7] MOSBY L. Ground loads for aircraft with multiple wheels and multiple landing gear and with requirements for semi-improved airfield operations[C]//Proceedings of Low-Speed Flight Meeting. Montreal, Canada: AIAA, 2012: 711.

[8] QIAN Xiaomei. Simulation study on nose wheel steering characteristics of aircraft[D]. Nanjing: Nanjing University of Aeronautics and Astronautics, 2008. (in Chinese)

[9] SHI X Z, NIE H, ZHANG M, et al. Six-wheel trolley type landing gear ground slip-Run load analysis considering fuselage flexibility[M]//Advances and Challenges in Advanced Unmanned Aerial Systems. Singapore: Springer Nature Singapore, 2024: 211-219.

[10] SHE C F, ZHANG M, HINKKANEN M, et al. An integrated design methodology for architecture solutions to shimmy reduction subsystems in all electric aircraft[J]. IEEE Transactions on Transportation Electrification, 2024, 10(4): 10428-10440.

[11] SHE C F, ZHANG M, GE Y B, et al. Design and simulation analysis of an electromagnetic damper for reducing shimmy in electrically actuated nose wheel steering systems[J]. Aerospace, 2022, 9(2): 113.

[12] ZHANG Ming, WEI Xiyang, YANG Zimin, et al. Six-wheel trolley type landing gear ground load analysis study[J]. Journal of Northwestern Polytechnical University, 2022, 40(5): 1090-1099. (in Chinese)

[13] BARNES A, YAGER T. Simulation of aircraft behaviour on and close to the ground: AGARD-AG-285 [R]. [S.l.]: Maritime Technical Information Facility. 1985.

[14] GAMEZ A, AL-QADI I L. Turning maneuver effect on near-surface airfield pavement responses[J]. Transportation Research Record: Journal of the Transportation Research Board, 2019, 2673(8): 275-283.

[15] LI Jing, YANG Shihai, GENG Jikai, et al. Design of angle control law for wide-body aircraft in ground main wheel cooperative turning[J]. Flight Control and Detection, 2024, 7(3): 15-21. (in Chinese)

[16] XIE Shuai, YANG Quanwei. An analysis and prediction of ground turning loads of multi-wheel and multi-strut landing gear[J]. Journal of Air Force Engineering University, 2022, 23(5): 22-27. (in Chinese)

[17] SHE C F, ZHANG M, HINKKANEN M, et al. Damping coefficient characterization and experiment of an electromagnetic damper for shimmy reduction[J]. ASME Transactions on Mechatronics, 2024, 30(3): 2017-2027.

[18] HOU Y X, GUAN Y L, JIA H G. Research on motion characteristics for UAV ground maneuvers[C]//Proceedings of 2015 IEEE International Conference on Mechatronics and Automation (ICMA). Beijing, China: IEEE, 2015: 22-26.

[19] KHAPANE P D. Simulation of asymmetric landing and typical ground maneuvers for large transport air-

craft[J]. Aerospace Science and Technology, 2003, 7(8): 611-619.

[20] CURREY N S. The C-5A landing gear[J]. SAE Transactions, 1968, 76(3): 2085-2098.

[21] LI Dongying. Research on ground loads of aircraft with multi-wheels and multi-landing gear based on virtual prototyping[D]. Nanjing: Nanjing University of Aeronautics and Astronautics, 2009. (in Chinese)

[22] JIANG Baiying, SHI Yongqiang, GUO Zhaodian. Research on large aircraft ground steering control method[J]. Aeronautical Science and Technology, 2015, 26(6): 62-65. (in Chinese)

[23] SHI X Z, NIE H, ZHANG M, et al. Kriging-assisted valid-screening optimization (KVSO) to study optimal steering strategies for multi-struts aircraft[J]. Aerospace Science and Technology, 2025, 162: 110157.

[24] YIN Q Z, KONG D X, SONG J Y, et al. Influence of asymmetrical factors on aircraft ground steering stability[J]. Aerospace Science and Technology, 2023, 142: 108698.

[25] SONG L, YANG H, YAN X F, et al. A study of instability in a miniature flying-wing aircraft in high-speed taxi[J]. Chinese Journal of Aeronautics, 2015, 28(3): 749-756.

[26] LIANG T T, YIN Q Z, WEI X H. Effects of landing gear layout on the safe rollout envelope of equipped-skid aircraft[J]. Aerospace Science and Technology, 2022, 122: 107434.

Acknowledgements This research was supported in part by the Fundamental Research Funds for the Central Universities (No.NP2022416) and the Aeronautical Science Foundation of China (No.2022Z029052001).

Authors

The first author Mr. **GUI Xiwen** received his B.S. degree in aircraft manufacturing engineering from Chongqing Jiaotong University in 2023. He is currently pursuing his Ph.D. degree in Nanjing University of Aeronautics and Astronautics. His research interests include multi-wheel landing gear, aircraft ground steering dynamics, coordinated steering.

The corresponding author Prof. **ZHANG Ming** received his Ph.D. degree in aircraft design from Nanjing University of Aeronautics and Astronautics (NUAA), China, in 2009. In June 2009, he joined Key Laboratory of Fundamental Science for National Defense-Advanced Design Technology of Flight Vehicle, College of Aerospace Engineering, NUAA, Nanjing, China. His research interests include aircraft design, dynamics and landing gear system.

Author contributions Mr. **GUI Xiwen** designed the study, analyzed the study, interpreted the results, and wrote the manuscript. Prof. **ZHANG Ming** implemented the model and revised the manuscript. Mr. **SHI Xiazheng** analyzed the result. Mr. **HU Tianyang** contributed to the discussion and background of the study. Mr. **XU Yuhan** contributed to the dynamics simulation. All authors commented on the manuscript draft and approved the submission.

Competing interests The authors declare no competing interests.

(Production Editor: ZHANG Bei)

多轮起落架随动转弯性能分析研究

桂熙汶[1]，张　明[1,2]，史夏正[1]，胡天洋[1]，徐宇晗[1]

(1.南京航空航天大学航空航天结构力学及控制全国重点实验室，南京 210016，中国；
2.南京航空航天大学飞行器先进设计技术国防重点学科实验室，南京 210016，中国)

摘要：在大型运输机地面转弯过程中，前起落架轮胎常常因承受过大侧向载荷而易发生侧滑，既影响转弯安全性，又加剧轮胎磨损。为解决这一问题，后排起落架通常与前轮随动转向，以减少轮胎侧滑并增强飞机的转弯机动性。本文探讨了起落架结构参数及重量分布参数对起落架随动转弯性能的影响。以C-5运输机为研究对象，构建了包含主起落架偏转的多轮飞机地面转弯动力学模型；建立了地面操纵动力学模型，探讨了随动转弯方式下后排主起落架的转弯性能提升收益。结果表明：当C-5采用后排主轮随动转弯后，前起各轮胎侧向摩擦系数分别减小22%、24%、26%、27%，飞机转弯半径减小了29.7%，前起转弯力矩减小了19%，转弯性能得到了明显提高。因此在大型运输机起落架设计过程中，应该以主起随动转弯方式、最优结构参数、最优重心位置参数为设计目标。研究结果为多轮大型运输机起落架的设计提供了理论依据。

关键词：多轮起落架；随动转弯；飞机地面转弯动力学；影响规律分析